HEAT TRANSFER ENHANCEMENT OF STAGGERED WATER-DROPLET GROOVED MICROCHANNEL HEAT SINK USING Al_2O_3 NANOFLUID

Yan Hao SOO[1], Kok Hwa YU[1,*], Mohd Azmi ISMAIL[1]

[1] School of Mechanical Engineering, Engineering Campus, Universiti Sains Malaysia, 14300 Penang, Malaysia

[*] Corresponding author; E-mail: yukokhwa@usm.my

The performance reliability and durability of modern cutting-edge technology are highly dependent on the ability of the devices to dissipate enormous amounts of heat to the ambient environment. A synergetic combination of two passive heat transfer enhancement techniques would be favourable to prevent overheating. The concurrent implementation of Al₂O₃ nanofluid and staggered water-droplet groove geometries in microchannel heat sink application was investigated using numerical approach. Numerical results reported in this study revealed that the heat dissipation capability of the microchannel heat sink can be improved when Al₂O₃ nanofluid is used in conjunction with the water-droplet grooves arranged in staggered manner. The predictive accuracy of the numerical method has been validated with published results available.

Keywords: *Computational Fluid Dynamics (CFD), Conjugate heat transfer, Microchannel heat sink, Nanofluids*

1. Introduction

The rapid miniaturization of electronic packaging has intensified the need for a more effective heat dissipation method to ensure that unwanted heat can be extracted from confined spaces, and this has driven the trends towards the development of novel cooling methods. The idea of using a microchannel heat sink for electronic cooling applications was first put forward by Tuckerman and Pease [1] through their ground-breaking experimental investigation on the performance of water-cooled microchannel heat sinks (MCHS) which consists of a spanwise periodic array of channels with identical geometric features that permit the passage of coolant to dissipate unwanted heat to the ambient environment. Since then, much effort has been exerted to augment the performance of the MCHS and among them, the channel geometry modification technique is the most preferred option to improve the heat removal capability of the MCHS [2-4].

Most earlier studies on MCHS applications rely on the conventional geometrical modification approach to augment the heat removal capability of the MCHS. However, the applicability of such techniques is often limited by physical design constraints which can only be mitigated by enhancing the transport properties of the working fluids. Furthermore, the overall cooling performance of the MCHS may also be affected by the transport properties of the coolant. The utilization of fluid additives has been proven to be an effective alternative to geometrical alteration where noticeable enhancement in thermal attributes was observed as compared with the conventional working fluid, as reported in the findings from several landmark studies [5-9].

The idea to improve the thermal properties of fluids through the colloidal suspensions of highly-conductive metallic particles was conceptualized by Maxwell [10] in his ground-breaking experimental work. However, the negative aspects associated with the augmentation has limited the practical application of such method. The rapid advancement of nanotechnology in the recent years has motivated researchers to revisit this approach. The utilization of nanofluids for heat transfer augmentation in MCHS was first popularised by the numerical investigation conducted by Jang and Choi [11] where a water-based nanofluid comprising 6 nm copper-nanoparticles and 2 nm diamond-nanoparticles was deployed as coolant in a MCHS. Back then, it was considered as an extension to the ground-breaking discovery of the potential of nanofluids in the mid-90s and the findings obtained exhibited a remarkable agreement with the premise. It was revealed that the cooling performance was enhanced by about 10 % as compared with the MCHS which used water as coolant for a fixed pumping power of 2.25 W.

Chein and Huang [7] investigated the potential of using nanofluid as a coolant to enhance the heat transfer of two specific MCHS geometries which are both made of silicon. With merely a 2 % addition of Cu nanoparticles, the thermal resistance of the MCHS reduces from 0.086 K/W to 0.06 K/W with no significant increase in pressure drop. This corresponds to a 30.23 % reduction in comparison to that using water as coolant. The augmentation in heat transfer is due to thermal conductivity enhancement and nanoparticle thermal dispersion. With the assumption that heat transfer enhancement could be enhanced by the addition of nanoparticles, Chein and Chuang [9] conducted experiments on silicon MCHS using $CuO\text{-}H_2O$ nanofluid to verify their theoretical prediction. The findings from experimental verification indicated that at a lower flow rate, the nanofluid-cooled MCHS could dissipate more heat than the water-cooled MCHS which then reduces the wall temperature to a lower level. In spite of that, the efficacy of the nanoparticles diminishes at higher flow rate due to the fact that the heat transfer was dominated by volume flow rate and the presence of nanoparticles did not contribute to extra heat dissipation. Moreover, they also revealed that the pressure losses in the microchannels increase slightly in the presence of nanoparticles.

Ho et al. [12] reported his experimental findings concerning the hydrothermal characteristics of alumina-water nanofluid in a copper MCHS. They discovered that the nanofluid-cooled MCHS exhibited a significant reduction in maximum wall temperature thermal resistance albeit with a marginal increase in friction factor as compared with pure water. In fact, the performance is better than that cooled by pure water at high pumping power. However, it was found that the decrease in effective specific heat capacity would counteract the benefits of the enhanced effective thermal conductivity. Farsad et al. [13] developed a three-dimensional numerical model to investigate the conjugate fluid flow and heat transfer behaviours of three different water-based nanofluids (i.e., Al_2O_3/water, CuO/water, and Cu/water) in an irregular MCHS formed by diffusion bonding of five copper sheets with identical thickness. The heat generated from the electronic device is dissipated through the zig-zag channels with the aid of nanofluids passage. The Cu/water nanofluids has higher effective thermal conductivity and hence yielded a better cooling performance as compared with the oxide metal nanofluids. The enhancement in heat dissipation performance is reported to be around 8.4 % and 9.6 % for Al_2O_3/water and CuO/water nanofluids, respectively.

Using numerical method, Hung et al. [14] conducted a comprehensive study on a nanofluid-cooled MCHS to examine every aspect of the heat sink and nanofluid which includes the effects of using different nanoparticles, base fluids, and substrate materials on the heat transfer performance. It

was found that the thermal resistance of the MCHS first decreases and then increases as the nanoparticle volume fraction increases. Ebrahimi et al. [15] evaluated the heat dissipation performance of a uniformly heated MCHS which used water-based nanofluid with cylindrical-shaped Multi-walled Carbon Nanotube suspension as coolant. The water-based fluid suspension which contains dispersed carbon nanotube nanoparticles were able to augment the heat removal performance by about 10 % and 4 % as compared with the other two cases which contain the exact concentration of diamond and copper nanoparticles. Colangelo et al. [16] employed Al_2O_3 nanofluid as the working fluid for the solar thermal collector, converting solar energy to thermal energy. It is reported that the thermal energy efficiency increased by approximately 3 %, when nanofluid with 1 % volume fraction of Al_2O_3 nanoparticle is employed.

To the best knowledge of the authors, to date, no systematic studies have been conducted on MCHS with staggered water-droplet geometries (SWG) to examine the effects of Al_2O_3 nanofluid application on heat transfer augmentation. The present study intends to evaluate the thermodynamic gain of using Al_2O_3 nanoparticle as additive to the base fluid in conjunction with the conventional geometrical modification techniques using staggered water-droplet grooved geometries. Apart from that, the present study also intends to correlate some of the most important parameters related to nanofluid application with the thermo-hydraulic characteristics of nanofluids in MCHS. To quantify the extent of heat transfer augmentation induced by the addition of Al_2O_3 nanoparticle, the performance of the staggered water-droplet geometries microchannel heat sink (SWG-MCHS) is benchmarked against the conventional microchannel heat sink (CON-MCHS) throughout this study.

2. Methodology

2.1. Geometrical configuration and boundary condition

The present study considers a microchannel heat sink with a footprint of 25 mm x 25 mm which comprises 24 rows of microchannels. Having parallel fins across the lateral direction, this gives rise to a periodic flow and thermal profiles across the microchannels. With such periodicity patterns in the lateral direction, this thus permits the simplification of the simulation model of an entire microchannel heat sink to a single microchannel periodic unit. Fig. 1 shows the schematic of the simplified computational domain which consists of a complete fluid domain bounded by two opposite halves of the solid domain, with a channel length of 25 mm and periodic width of 1 mm. In addition, both the fin and the channel have equal width of 500 μm. In this study, MCHS with water-droplet grooves patterned along the side walls are considered. In this study, each periodic unit consists of 10 transitional repetitive pairs of water-droplet grooves along the side walls, as illustrated in Fig. 2. The pitch length of each repetitive unit (L_p) is thus 2.5 mm. As can be seen from this figure, a repetitive unit contains a pair of water-droplet grooves. For each repetitive unit, the water-droplet grooves are arranged in a staggered manner with one placed in the upstream with the focal point of the water-droplet groove being positioned at a quarter pitch length (i.e., $L_p/4$) from the upstream boundary. Meanwhile, the subsequent groove is placed at the adjacent wall at the downstream with three-quarters of the pitch length (i.e., $3L_p/4$) from the upstream boundary. It should be noted that the leading edge radius of the water-droplet groove L_{r1} of 100 μm and trailing edge radius of the water-droplet groove L_{r2} of 200 μm are adopted throughout this study. Additional details pertaining to the MCHS bulk dimensions are stated in Tab. 1. The MCHS substrate is made of copper with its thermo-

physical properties are regarded as constants: density ρ_s, thermal conductivity k_s, and specific heat capacity at constant pressure c_s of which are $8978\,\text{kg/m}^3$, $387.6\,\text{W/mK}$, and $381\,\text{J/kgK}$, respectively.

Table 1. Bulk dimensions of the MCHS

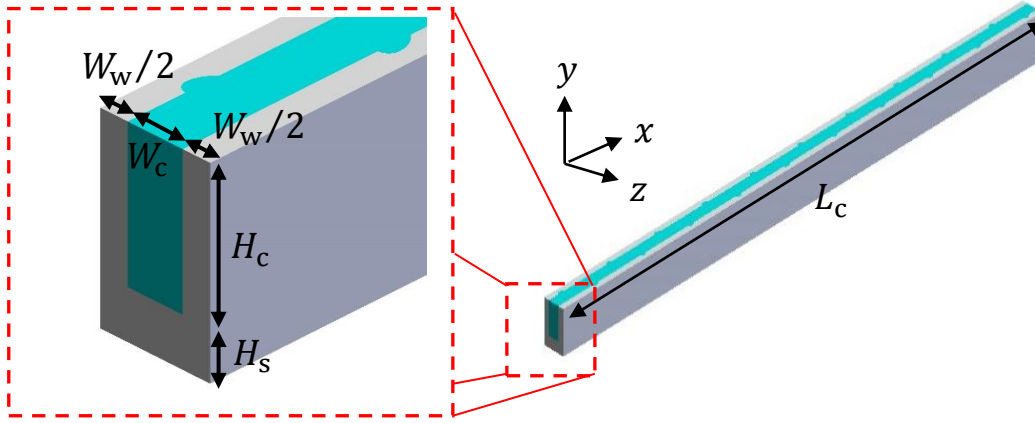| Parameters	Dimensions
Channel length, $L_c(\mu m)$	25000
Channel width, $W_c(\mu m)$	500
Fin width, $W_w(\mu m)$	500
Channel depth, $H_c(\mu m)$	1500
Aspect ratio, AR (dimensionless)	3
Thickness of substrate, $H_s(\mu m)$	500
Hydraulic diameter, $D_h(\mu m)$	750

Figure 1. Isometric view of staggered water-droplet grooved MCHS.
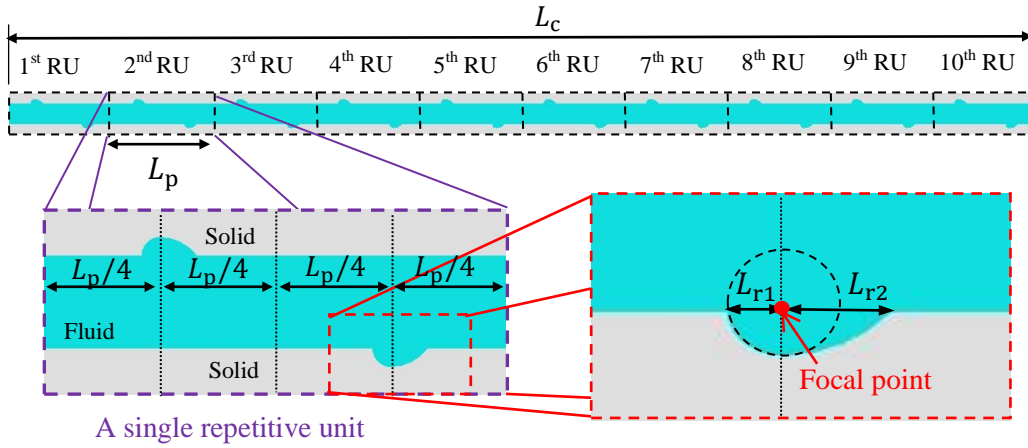

Figure 2. Top view of the simplified computational domain.

4

Table 2. Boundary conditions imposed on the computational domain

Location	Hydrodynamic BC	Thermal BC
Inlet	Constant inlet velocity	Inlet temperature of 293 K
Outlet	Pressure outlet with gauge pressure of 0 Pa	-
Top surface	No-slip wall	Adiabatic
Base of substrate	No-slip wall	Constant heat flux of 6.5×10^5 W/m^2
Left & right surface	Translational periodic	Translational periodic
Solid-liquid interface	No-slip wall	System coupling

A uniform velocity is imposed in the range of 0.2 m/s to 1.0 m/s and a fixed fluid temperature of 293 K is specified at the microchannel inlet. At the microchannel outlet, a gauge pressure of 0 Pa is specified. At the heat sink substrate base, a uniform heat flux of 6.5×10^5 W/m^2 is prescribed to emulate the dissipated heat from a heat source such as electronic chip [3]. The rigid wall assumption and no-slip boundary conditions are applied to all wall surfaces. At the side boundaries, a periodic boundary condition is adopted. It is also worth to note that the system coupling boundary condition is chosen for all solid-liquid interfaces. Unless mentioned otherwise, the remaining wall surfaces (including top surface) are assumed to be perfectly insulated and adiabatic boundary condition is imposed on these surfaces. The boundary conditions imposed were summarized in Tab. 2.

2.2. Governing equations

The state of the coolant across the microchannel is treated as incompressible Newtonian laminar flow, regardless of the nanoparticle concentration. Apart from that, the flow is also assumed to obey the continuum assumption and the effects of gravitational force, radiation heat transfer, and viscous dissipation are all neglected. The energy equations in the fluid and solid domains are solved simultaneously using the conjugate heat transfer approach which combines heat conduction in solid domain with heat convection in fluid domain. A single-phase fluid model which assumes thermal equilibrium and zero relative velocity between base fluid and nanoparticles are used to model the force convective heat transfer behaviour of nanofluid.

The governing equations for conservations of mass, momentum, and energy are defined as follows.

Continuity equation: $\quad \nabla \cdot \left(\rho_{\mathrm{nf}} \vec{V} \right) = 0,$ (1)

Momentum equation: $\quad \nabla \cdot \left(\rho_{\mathrm{nf}} \vec{V} \vec{V} \right) = -\nabla p + \nabla \cdot \left(\mu_{\mathrm{nf}} \nabla \vec{V} \right),$ (2)

Energy equations: $\quad \nabla \cdot \left(\rho_{\mathrm{nf}} \vec{V} \, c_{\mathrm{nf}} \, T_{\mathrm{nf}} \right) = \nabla \cdot \left(k_{\mathrm{nf}} \nabla \, T_{\mathrm{nf}} \right),$ (fluid) (3)

$\quad \nabla \cdot \left(k_{\mathrm{s}} \nabla \, T_{\mathrm{s}} \right) = 0.$ (heat sink substrate) (4)

5

The density, pressure, and dynamic viscosity are represented by ρ, p, and μ, respectively. The velocity field is denoted as $\vec{V}$. The temperature, specific heat capacity at constant pressure, and thermal conductivity are denoted by T, c, and k, respectively. The subscripts nf and s refer to the coolant and heat sink substrate, respectively.

2.3. Thermo-physical properties of Al_2O_3 nanofluid

The Al_2O_3 nanofluid is implemented as coolants and the volume concentration of nanoparticles considered are 0 %, 2 %, and 4 %. The expressions used to predict the effective thermo-physical properties of Al_2O_3 nanofluid are presented in Eqs. (5), (6), (7), and (9) while the thermo-physical properties of water at 293 K are presented, in Tab. 3. For Al_2O_3 nanoparticle, the density, specific heat capacity, and thermal conductivity, are 3970 kg/m^3, 765 J/kgK, and 40 W/mK, respectively [17]. Tab. 4 tabulates the effective thermo-physical properties of the Al_2O_3 nanofluid for nanoparticle volume fraction at 2 % and 4 %. The formulations that takes into account the composition dependency of nanofluid (Eqs. (5), (6), (7), and (9)) are implemented using User-Defined Function (UDF) to estimate the effective thermo-physical properties of nanofluid. It should be noted that the thermo-physical properties of the heat sink and nanofluid are temperature independent.

Table 3. Thermo-physical properties of water at T = 293 K.

Properties	Values
Density (kg/m^3)	998.2
Specific heat capacity (J/kgK)	4182
Thermal conductivity (W/mK)	0.613
Dynamic viscosity (kg/ms)	0.001003

Table 4. Effective thermo-physical properties of Al_2O_3 nanofluid at T = 293 K.

Nanofluid	Nanoparticle volume fraction, $\emptyset(\%)$	Density, ρ_{nf} (kg/m^3)	Specific heat capacity, c_{nf} (J/kgK)	Thermal conductivity, k_{nf} (W/mK)	Dynamic viscosity, μ_{nf} (kg/ms)
$Al_2O_3 - H_2O$	2.0	1057.64	3925.48	0.6488	0.001053
	4.0	1117.07	3696.25	0.6861	0.001103

The expression used to predict the effective density of the nanofluid is derived from the law of mixture and it is given as [18]

$$\rho_{nf} = (1 - \emptyset)\rho_{bf} + \emptyset\rho_{np}, \tag{5}$$

where the Greek symbol $\emptyset$ refers to the volume fractions/concentrations of nanoparticles in the nanofluids. The subscript nf, bf and np refer to nanofluid, base fluid, and nanoparticle, respectively. The formulation was validated by Pak and Ho [19] through the experimental collections of Al_2O_3-water nanofluid density measurements at room temperature concerning different nanoparticle volume fractions. Both experimental results yielded excellent agreement with the theoretical predictions.

The expression used to predict the effective specific heat of the nanofluid, and constant pressure [18] is based on the assumption that both base fluid and nanoparticles are in a state of thermal equilibrium and it is given as

$$C_{nf} = \frac{(1 - \emptyset)(\rho c)_{bf} + \emptyset(\rho c)_{np}}{\rho_{nf}}. \tag{6}$$

The effective thermal conductivity of the nanofluid is computed using the empirical correlation suggested by [10]

$$k_{nf} = \frac{k_{np} + 2k_{bf} + 2\emptyset_{np}(k_{np} - k_{bf})}{k_{np} + 2k_{bf} - \emptyset_{np}(k_{np} - k_{bf})} k_{bf}. \tag{7}$$

The Maxwell model [10] was obtained by solving the heat conduction equation through a stationary arbitrary dispersion of spherical particles. It is first-order accurate and can be applicable to nanofluids with $\emptyset_{np} \ll 1$ or $|k_{np}/k_{bf} - 1| \ll 1$. Interestingly, the predictions from the Maxwell model coincide with those acquired from the Hamilton-Crosser model [20] which incorporates an empirical shape factor given by $n = 3/\psi$.

$$k_{nf} = \frac{k_{np} + (n - 1)k_{bf} + (n - 1)\emptyset_{np}(k_{np} - k_{bf})}{k_{np} + (n - 1)k_{bf} - \emptyset_{np}(k_{np} - k_{bf})} k_{bf}. \tag{8}$$

The ψ refers to the particle sphericity, defined as the ratio of sphere surface area to the particle surface area. The shape of the nanoparticles is assumed to be spherical in the context of the present study which hence gives a sphericity of 1 and a resulting empirical shape factor of 3. By substituting the empirical shape factor into the expression, the Hamilton-Crosser model can be simplified into the same expression as in the Maxwell model. The Hamilton-Crosser model was not the only apparition of the Maxwell model. In fact, there is another physical model known as the Wasp model [21] which has an identical expression as the Maxwell model. The effective viscosity of the nanofluid is obtained using the following formulation as provided in [22]

$$\mu_{nf} = \mu_{bf}(1 + 2.5\emptyset_{np}) \tag{9}$$

The Einstein's model [22] for effective viscosity is applicable for dilute suspension of rigid spheres in a viscous liquid with volume concentration lower than 5 %. The expression was obtained by solving the hydrodynamic equations and it assumed that there is no interaction between the suspended spherical nanoparticles.

The partial differential equations which describe the behaviour of the Al_2O_3 nanofluid along the microchannels are solved using commercial finite volume numerical solver: ANSYS Fluent 2022 R1. The SIMPLE (Semi-Implicit Method for Pressure-Linked Equations) algorithm is implemented for pressure-velocity coupling. Green-Gauss Node Based and Second-order scheme are selected for the spatial discretization of gradient and pressure. Second-order Upwind scheme is used for the spatial discretization of momentum and energy. The CFD simulations are computed by a double-precision serial solver running on a 4 cores Intel® Xeon® CPU E3-1226v3, 12GB RAM workstation. The solution is considered as converged when the scaled residuals of the continuity, momentum, and energy equations are less than the prescribed value of 10^{-6}.

The following section presents the measurement approaches employed to quantify the extent of performance enhancement brought by the inclusion of staggered water-droplet grooves in a

rectangular microchannel. The Reynolds number (Re) and hydraulic diameter (D_h) are defined as follows.

$$\text{Re} = \frac{\rho V D_h}{\mu},$$ (10)

$$D_h = \frac{2(H_c W_c)}{H_c + W_c},$$ (11)

where the terms of ρ, V, μ, H_c, and W_c refer to density, inlet velocity, dynamic viscosity, channel height, and channel width, respectively. The enhancement in thermal performance is evaluated by assessing the reduction of thermal resistance which is given by

$$R = \frac{T_{\max} - T_{\text{in}}}{q'' A_b},$$ (12)

where the terms of $T_{\max}$, T_{in}, q'', and A_b denote the maximum temperature of the MCHS substrate, the inlet temperature of the coolant, the heat flux applied at the substrate base, and the surface area of the substrate base, respectively.

Meanwhile, the pumping power (P) across the heat sink can be computed using Eq. (13) by taking the sum of products of the pressure drop and the volumetric flow rate of the microchannels. The pressure drop of coolant across the microchannel which is denoted by Δp is calculated by taking the difference between the mass-weighted average values of total pressures at the microchannel inlet and outlet. The term $\dot{V}$ refers to the volumetric flow rate of the coolant.

$$P = \Delta p \dot{V}.$$ (13)

In practical application, the electrical power needed to produce the desired flow conditions in this study can be computed based on the attained pumping power in Eq. (13) and the efficiency of a given pump.

3. Results and discussion

3.1. Validation of the numerical method

The numerical model was validated to ascertain the accuracy of the numerical model employed in producing reliable results by comparing the attained results with the experimental data reported by Lee et al. [23]. For this validation, following the geometries stated in Lee et al. [23], a single unit of conventional MCHS model of channel depth of 1482.2 μm, channel width of 547 μm, and fin width of 458.5 μm was simulated. At the bottom of the heat sink, a constant heat flux of 6.5×10^5 W/m^2 is imposed. Meanwhile, the water inlet temperature is specified to be 293 K. As can be observed from Fig. 3, the numerical results for both temperature difference ($\Delta T = T_{\text{out}} - T_{\text{in}}$) and pressure drop ($\Delta P = P_{\text{in}} - P_{\text{out}}$) are in good agreement with the experimental data of Lee et al. [23]. For Reynolds numbers ranging between 300 and 800, in corresponding to the inlet velocity of approximately 0.3 m/s and 0.9 m/s, the average deviation for ΔP between present numerical simulation results and that of experimental data of Lee et al. [23] is approximately 15 %. This is comparable to the numerical results reported by Lee et al. [23], with average deviation of 12%. In terms of temperature difference ΔT, the average deviation is less than 10 %, comparing the results

from present numerical results with the experiment data. It is worth to note that the numerical results of Lee et al. [23] on temperature difference ΔT is not explicitly available.
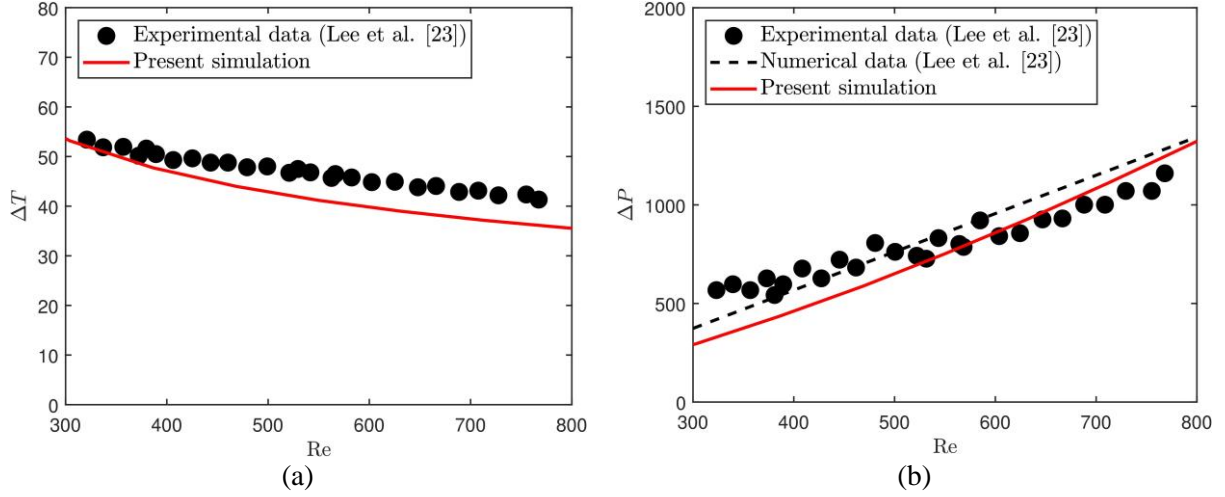

Figure 3. Comparison of present simulation with experimental data of Lee et al. [23] on (a) temperature difference and (b) pressure drop, attained for conventional MCHS, for Reynolds number ranging from 300 to 800.
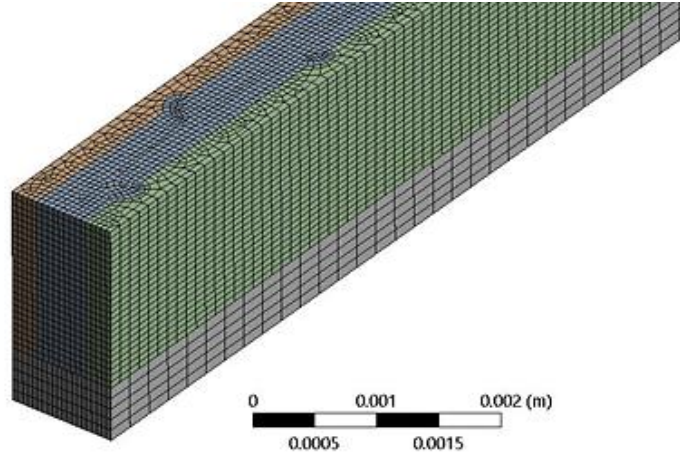
3.2. Grid independence test

Figure 4. Illustration of grid generation for staggered water-droplet grooved MCHS.

As depicted in Fig. 4, mixed structured and unstructured hexahedral grids are generated to mesh the computational domains using ANSYS Meshing with finer grid resolution applied to the fluid domain. The variations in both R and P are assessed for different grid resolutions (i.e., M1 to M4). The mesh convergence test evaluated is based on the relative error metric to ensure that the solutions obtained are independent of the computational grid resolution. The relative errors for both thermal resistance and pumping power are computed using the following equation.

$$e_R = \left| \frac{R_{M_x} - R_{M_4}}{R_{M_4}} \right| \times 100\%, \tag{14}$$

$$e_P = \left| \frac{P_{M_x} - P_{M_4}}{P_{M_4}} \right| \times 100\%, \tag{15}$$

in which e represents the relative error obtained from the result of the pertained grid resolution in comparison to the one obtained from the grid resolution of M4. Tab. 5 shows the relative errors of thermal resistance and pumping power for different grid resolutions with respect to the finest grid resolution M4 used. The results pertaining to grid independence test is corresponding to pure water driven at constant inlet velocity of 0.2 m/s. Meanwhile, Fig. 5 shows the variation of the resulted thermal resistance and pumping power with respect to the number of elements used. The grid resolution M3 with 184325 elements employed exhibits reasonable accuracy for both R and P. The deviation is found to be less than 0.3 % for R when compared with that of M4 which has a resolution of 290530 elements. More appalling, the deviation for P is merely 0.06 %. As such, the grid resolution M3 is preferred and thus it is adopted for the subsequent studies in this paper.

Table 5. Relative error in thermal resistance and pumping power with respect to the finest grid.

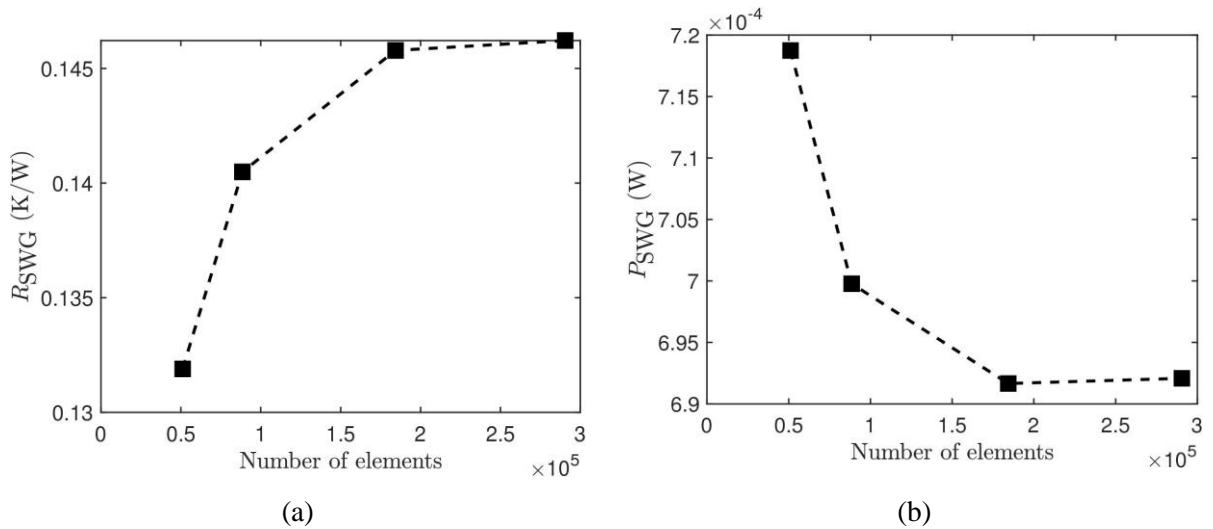| Grid	Number of elements	Thermal resistance $R(K/W)$	Relative error $e_R(\%)$	Pumping power $P(W)$	Relative error $e_P(\%)$
M1	51130	0.1319	9.79	0.0007187	3.85
M2	88489	0.1405	3.92	0.0006998	1.11
M3	184325	0.1458	0.29	0.0006917	0.06
M4	290530	0.1462	Baseline	0.0006921	Baseline

Figure 5. Grid independence test on (a) thermal resistance and (b) pumping power for SWG-MCHS.

3.3. Effect of water-droplet grooves

Fig. 6 shows velocity vectors and temperature contour plots for fluid flow at the downstream (i.e., 0.015 m $\leq x \leq$ 0.025 m) of conventional microchannel heat sink (CON-MCHS) and staggered water-droplet grooved microchannel (SWG-MCHS). The results depicted in this figure is

corresponding to pure water (using 0 % volume fraction of nanoparticle) driven at constant inlet velocity of 0.2 m/s. The thermal contour plots are extracted at the midplane which is half of the heat sink height (i.e., 1000 μm from the bottom of the heat sink). As can be observed from this figure, the maximum temperature at this plane is noticeably lower for SWG-MCHS as compared with the CON-MCHS. On this plane, the maximum temperatures are 356.7 K and 354.0 K, for CON-MCHS and SWG-MCHS, respectively. The reduction on the temperature of the microchannel can be attributed to the presence of the water-droplet grooves which allows flow in the cavities. When water flows in the vicinity of the grooves, the water separates from the main flow at the core and it is then diverted into the grooves due to the sudden cross-section expansion of the flow path in the transverse direction. With the flow circulation created in the grooves, this gives rise to better heat dissipation for the SWG-MCHS.
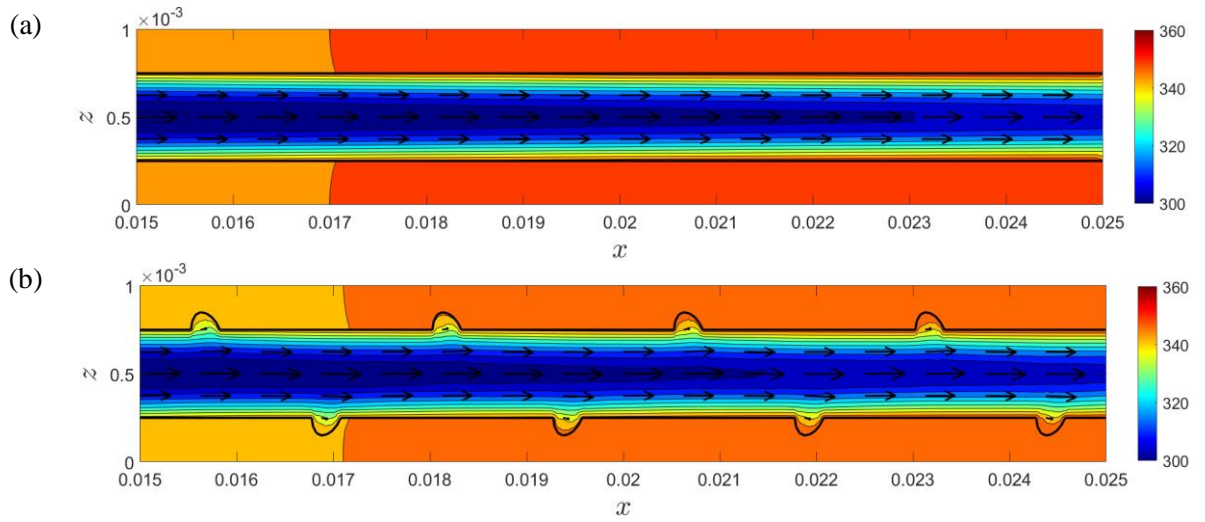

Figure 6. Velocity vectors and temperature contour plots for (a) CON-MCHS, and (b) SWG-MCHS with water flow at 0.2 m/s.

3.4. Effect of Al_2O_3 nanoparticle concentration

As SWG-MCHS is deemed to be promising in dissipating heat, the heat transfer enhancement of this MCHS design is thus studied for different Al_2O_3 nanoparticle concentration. Fig. 7 depicts the effect of nanoparticle concentration and inlet velocity on the maximum temperature (T_{max}) for both CON-MCHS and SWG-MCHS. As can be observed from this figure, the maximum temperature is higher at lower fluid velocity and it is gradually lower when larger fluid velocity is employed. Comparatively, the maximum temperature on the MCHS is observed to be consistently smaller for the SWG-MCHS in comparison to the CON-MCHS, regardless of the fluid velocity and the nanoparticle volume fraction. For a MCHS, a lower maximum temperature implies that lower operating temperature of the MCHS is expected, thereby inferring a better heat dissipation performance. On the other hand, low thermal resistance (R) of the MCHS is desirable as it directly reflects the efficacy of heat dissipation. An increase in the nanoparticle volume fraction will lead to the increase of effective density, thermal conductivity, and viscosity, followed by a reduction in the effective heat capacity. It should be noted that the product of effective density and specific capacity of the nanofluid is always smaller than that of the base fluid regardless of the nanoparticle type which implies that the reduction

11

of thermal resistance is less dependent on the reduction of convective thermal resistance but relies significantly on the reduction of conductive resistance. The reduction of conductive resistance is achieved by minimizing the temperature difference between the Al_2O_3 nanofluid and the heat sink substrate base. At low inlet velocity, the diffusive heat transfer is more dominant due to the longer residence time of the coolant in the microchannels.
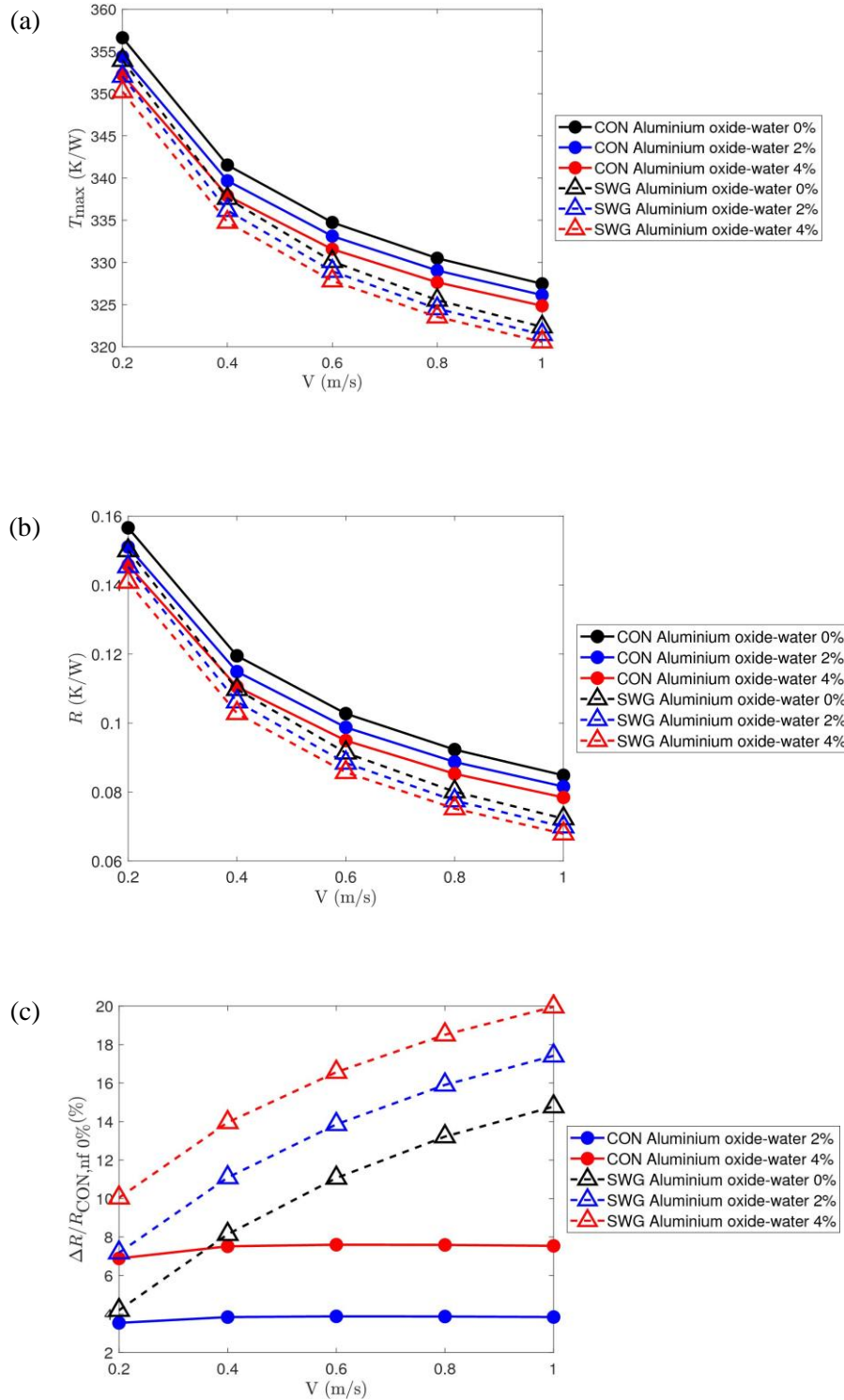

Figure 7. Variation of (a) T_{max}, (b) R, and (c) $\Delta R/R_{CON,nf\,0\%}$ with respect to inlet velocities for CON-MCHS and SWG-MCHS with different Al_2O_3 nanoparticle volume fractions.

12

On the other hand, the heat transfer due to the bulk motion of coolant is more dominant at a higher inlet velocity which results in a lower thermodynamic gain of the coolant at the microchannel outlets. As observed in Fig. 7, the thermal resistance (R) of SWG-MCHS is consistently lower as compared with that of the CON-MCHS, between which the maximum reduction is observed when water enters the microchannels at 1.0 m/s. In comparison to the CON-MCHS with pure water, the SWG-MCHS with pure water reduces the thermal resistance from 0.085 K/W to 0.072 K/W, equivalent to a 14.78 % reduction, as indicated by $\Delta R/R_{CON,nf\,0\%}$. By dispersing aluminium oxide nanoparticles into the water at 2 % and 4 % volume fractions, the SWG-MCHS further reduces it down to 0.07 K/W ($\sim 17.42\%$ reduction) and 0.068 K/W ($\sim 19.96\%$ reduction), respectively. Comparatively, at the same inlet velocity and volume fractions, the thermal resistances of the CON-MCHS are 0.082 K/W and 0.078 K/W which correspond to approximately 3.84 % and 7.54 % reduction. The rationale behind these observations is that the thermal conductivity of the base fluid is effectively enhanced through the suspension of low-volume fraction nanoparticles which in turn leads to an augmentation in heat absorption capability. Apart from that, the pronounced augmentation at higher volume concentrations can be attributed to the higher momentum of the nanoparticles. It is worth to note that, in practical condition, the upstream region of the microchannel flow may be subjected to the velocity and thermal developing flow regime. For channels considered in this study, the hydrodynamic entrance length is estimated to be $L_h \approx 0.05 \mathrm{Re} D_h$. For flow within 0.2 m/s to 1 m/s, the Reynolds number for flow in the microchannel studied is approximated to be between 150 to 750. For hydraulic diameter of 750 microns, the hydrodynamic entrance length is thus expected to be approximately between 5.6 mm to 28.1 mm. For thermal entrance length, $L_t \approx 0.05 \mathrm{Re}\mathrm{Pr} D_h$, almost the same channel length is expected. In developing flow region, the pressure drop is expected to be higher, thus inducing higher pumping power required. Similar trend is anticipated for thermal performance.

Apart from the thermal attributes, the conduciveness of Al_2O_3 nanoparticle as fluid additive to enhance the transport characteristic of the base fluid is examined from the aspect of energy consumption. The subject of energy consumption is of substantial importance, especially in the case where nanofluids are employed as a coolant because the addition of nanoparticles may intensify pressure losses which necessitate additional pumping power to overcome. A marked increase in pumping power expenditure is observed when the nanoparticle volume fraction is increased. The increase is because the coolant becomes more viscous with the addition of Al_2O_3 nanoparticles and has higher shear stress on the microchannel walls. Despite the resulting upsurge in pumping power consumption, the Al_2O_3 nanofluid-cooled MCHS outperformed the water-cooled MCHS. As depicted in Fig. 8, the pumping power expenditure (as indicated by $\Delta P/P_{CON,\,nf\,0\%}$) of CON-MCHS is consistently higher than that of the SWG-MCHS.

13

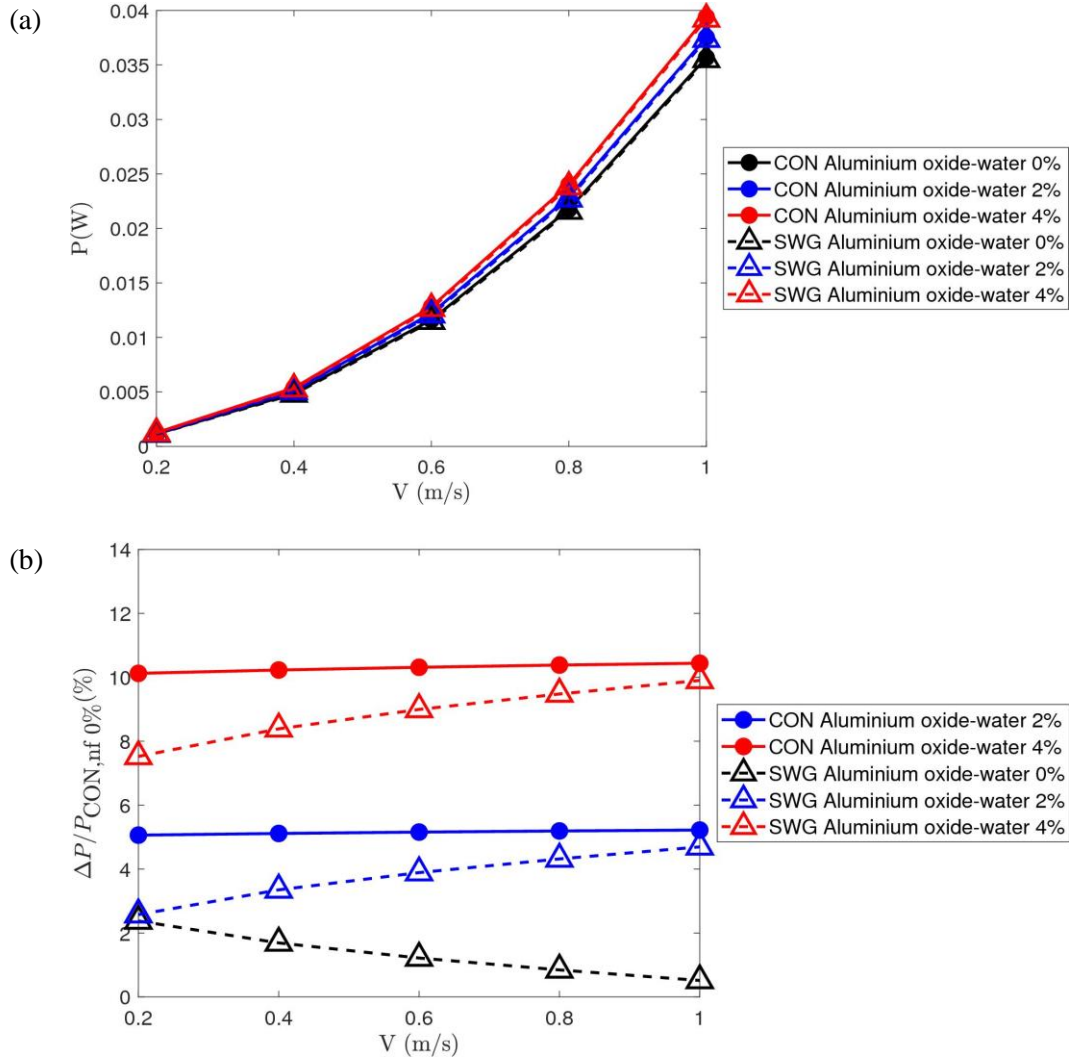**Figure 8.** Variation of (a) P and (b) $\Delta P/P_{CON,\,nf\,0\%}$ with respect to inlet velocities for CON-MCHS and SWG-MCHS with different Al_2O_3 nanoparticle volume fractions.

4. Conclusion

In this study, conjugate heat transfer numerical simulations were performed on CON-MCHS and SWG-MCHS using a single-phase approach to investigate the thermo-hydraulic performance of Al_2O_3 nanofluid flow. Two distinct passive heat transfer enhancement techniques (offset cavities and nanofluids) were implemented in the attempt to ameliorate the heat removal capability of the MCHS. The reduction of thermal resistance becomes more pronounced with the increase of nanoparticle concentration and coolant inlet velocity. Considerable reduction in the thermal resistance implies that the improvement of the MCHS heat dissipation performance is not merely attributed to the enhancement of effective thermal conductivity induced by nanoparticle addition but also due to the dependence of forced convective heat transfer augmentation on the flow velocity. Apart from that, the adoption of nanoparticles allows the coolant to extract more heat with minimal temperature gain. With that being said, the augmentation of heat removal is accompanied by the increase of pressure drop across the microchannel length which offsets the beneficial effect of Al_2O_3 nanofluid. This

corresponds to an upsurge in pumping power consumption due to its direct correlation with the pressure drop. Despite having a larger pumping power requirement, the implementation of Al_2O_3 nanofluid is preferable to water as the advantage on higher heat dissipation greatly outweigh the disadvantage of the additional pressure loss.

Acknowledgement

Nomenclature

A	Surface area (m^2)	*Subscript*	
AR	Aspect ratio	b	Heat sink base
c	Specific heat capacity (J/kgK)	bf	Base fluid
D	Diameter (μm)	c	Channel
e	Relative error (%)	con	Conventional microchannel heat sink
H	Depth/Thickness (μm)	h	Hydraulic
k	Thermal conductivity (W/mK)	in	Inlet
L	Length (μm)	max	Maximum
M	Mesh	nf	Nanofluid
P	Pumping power (W)	np	Nanoparticle
p	Pressure (Pa)	out	Outlet
Pr	Prandtl number	p	Pitch
q''	Heat flux (W/m^2)	r1	Leading edge radius
R	Thermal resistance (K/W)	r2	Trailing edge radius
Re	Reynolds number	s	Solid
T	Temperature (K)	w	Fin
$\vec{V}$	Velocity (m/s)		
$\dot{V}$	Volumetric flow rate (m^3/s)		
W	Width (μm)		

Greek symbol
Δ Difference
ρ Density (kg/m^3)
μ Dynamic viscosity (m^2/s)
$\emptyset$ Volume fraction of nanoparticles

REFERENCES

1. Tuckerman, D.B. and R.F.W. Pease, *High-performance heat sinking for VLSI*. IEEE Electron Device Letters, 1981. **2**(5): p. 126-129.
2. Abdelmohimen, M.A.H., et al., *Numerical investigation of using different arrangement of fin slides on the plate-fin heat sink performance*. Thermal Science, 2021. **25**(6): p. 4683-4693.
3. Choong, J.Y., K.H. Yu, and M.Z. Abdullah, *Numerical assessment on heat transfer performance of double-layered oblique fins micro-channel heat sink with al2o3 nanofluid* Thermal Science, 2022. **26**(1): p. 477-488.
4. Cong, B., et al., *Investigation on the heat dissipation of high heat flux chip array by fractal micro-channel networks*. Thermal Science, 2023. **27**(1): p. 869-880.
5. Jung, S.Y. and H. Park, *Experimental investigation of heat transfer of Al2O3 nanofluid in a microchannel heat sink*. International Journal of Heat and Mass Transfer, 2021. **179**: p. 121729.
6. Yang, L., et al., *Numerical assessment of Ag-water nano-fluid flow in two new microchannel heatsinks: Thermal performance and thermodynamic considerations*. International Communications in Heat and Mass Transfer, 2020. **110**: p. 104415.
7. Chein, R. and G. Huang, *Analysis of microchannel heat sink performance using nanofluids*. Applied Thermal Engineering, 2005. **25**(17): p. 3104-3114.
8. Tsai, T.-H. and R. Chein, *Performance analysis of nanofluid-cooled microchannel heat sinks*. International Journal of Heat and Fluid Flow, 2007. **28**(5): p. 1013-1026.
9. Chein, R. and J. Chuang, *Experimental microchannel heat sink performance studies using nanofluids*. International Journal of Thermal Sciences, 2007. **46**(1): p. 57-66.
10. Maxwell, J.C., *A treatise on electricity and magnetism*. A Treatise on Electricity and Magnetism. Vol. 9781108014038. 2010. 1-442.
11. Jang, S.P. and S.U.S. Choi, *Cooling performance of a microchannel heat sink with nanofluids*. Applied Thermal Engineering, 2006. **26**(17): p. 2457-2463.
12. Ho, C.J., L.C. Wei, and Z.W. Li, *An experimental investigation of forced convective cooling performance of a microchannel heat sink with Al2O3/water nanofluid*. Applied Thermal Engineering, 2010. **30**(2): p. 96-103.
13. Farsad, E., et al., *Numerical simulation of heat transfer in a micro channel heat sinks using nanofluids*. Heat and Mass Transfer, 2011. **47**(4): p. 479-490.
14. Hung, T.-C., et al., *Heat transfer enhancement in microchannel heat sinks using nanofluids*. International Journal of Heat and Mass Transfer, 2012. **55**(9): p. 2559-2570.
15. Ebrahimi, S., et al., *Cooling performance of a microchannel heat sink with nanofluids containing cylindrical nanoparticles (carbon nanotubes)*. Heat and Mass Transfer, 2010. **46**(5): p. 549-553.
16. Colangelo, G., M. Milanese, and A. De Risi, *Numerical simulation of thermal efficiency of an innovative Al2O3 nanofluid solar thermal collector influence of nanoparticles concentration*. Thermal Science, 2017. **21**(6): p. 2769-2779.
17. Mohammed, H.A., P. Gunnasegaran, and N.H. Shuaib, *The impact of various nanofluid types on triangular microchannels heat sink cooling performance*. International Communications in Heat and Mass Transfer, 2011. **38**(6): p. 767-773.
18. Khanafer, K. and K. Vafai, *A critical synthesis of thermophysical characteristics of nanofluids*. International Journal of Heat and Mass Transfer, 2011. **54**(19): p. 4410-4428.
19. Pak, B.C. and Y.I. Cho, *Hydrodynamic and heat transfer study of dispersed fluids with submicron metallic oxide particles*. Experimental Heat Transfer, 1998. **11**(2): p. 151-170.
20. Hamilton, R.L. and O.K. Crosser, *Thermal Conductivity of Heterogeneous Two-Component Systems*. Industrial & Engineering Chemistry Fundamentals, 1962. **1**(3): p. 187-191.
21. Wasp, E.J., R.L. Gandhi, and J.P. Kenny, *Solid-liquid flow: slurry pipeline transportation*. CLAUSTHAL, GERMAN FED. REPBL., TRANS TECH. PUBLICATIONS, 1977, 1975. **1 , 4.).**
22. Einstein, A., *Eine neue Bestimmung der Moleküldimensionen*. Annalen der Physik, 1906. **324**(2): p. 289-306.

23.   Lee, Y.J., P.S. Lee, and S.K. Chou, *Enhanced thermal transport in microchannel using oblique fins.* Journal of Heat Transfer, 2012. **134**(10): p. 101901.